High-temperature rheological behavior and non-isothermal pyrolysis mechanism of macerals separated from different coals

Yucen Kuang (况雨岑) [1,2], Tao Jiang (姜涛) [1,2], Longqi Wu (吴龙起) [1,2], Xiaoqian Liu (刘晓茜) [3], Xuke Yang (杨旭科) [1,2], Farooq Sher [4], Zhifang Wei (魏志芳) [1,2], Shengfu Zhang (张生富) [1,2*]

[1] College of Materials Science & Engineering, Chongqing University, Chongqing 400044, China

[2] Chongqing Key Laboratory of Vanadium-Titanium Metallurgy & Advanced Materials, Chongqing University, Chongqing 400044, China

[3] State Key Laboratory of Coal Mine Disaster Dynamics and Control, Chongqing University, Chongqing 400044, China

[4] Department of Engineering, Nottingham Trent University, Nottingham NG11 8NS, United Kingdom

First author:

Yucen Kuang, kuangyucen@cqu.edu.cn

*Corresponding author:

Shengfu Zhang, zhangsf@cqu.edu.cn

Abstract

It is a challenge to accurately characterize the caking behavior of coal after thermal softening and its reaction mechanism. In this work, the formation behavior of metaplast during coal macerals coking was investigated using high-temperature confocal laser scanning microscopy and high-temperature small-amplitude oscillatory shear rheometer, the source of diversities in thermal fluidity of coal was revealed by thermogravimetric-mass spectrometry analysis and kinetic-thermodynamic theory calculations. The results showed that although vitrinite was the generator of metaplast in the thermoplastic stage, the expansion rate of vitrinite from coking coal is more than 70% greater than that from gas coal for two consecutive times. Moreover, the total weight loss of vitrinite from gas coal was about 1.262 times higher than that from coking coal, but the latter exhibited more generous aliphatic groups in pyrolysis products. In the thermal flow interval, the reaction activation energy of vitrinite and inertinite from coking coal and gas coal was 271±0.7, 302±1.5, 241±0.1 and 300.25±1.55 kJ/mol, respectively. Eventually, the kinetic and thermodynamic mechanism parameters of raw coal and macerals had favorable correspondence regularity, and macerals with the most prominent parameters would be dominant in the overall thermal properties of raw coal.

Keywords: Coal macerals; Pyrolysis; Coking process; Metaplast; Rheological; Thermogravimetric

Nomenclature

Symbols

A^*	Ash content (%)
M	Moisture content (%)
V	Volatile content (%)
FC	Fixed carbon content (%)
ad	Air dry basis
$\bar{R}_{\max}$	Vitrinite reflectance value (%)
m/z	Mass/charge ratios (-)
α	Conversion rate (-)
m_0	Initial mass of the substance (mg)
m_t	Mass of the substance at moment t (mg)
m_∞	Mass of the pyrolysis end-temperature residue (mg)
A	Pre-exponential factor (1/min)

E_α	Reaction activation energy (kJ/mol)
$\bar{E}_{\alpha=x}$ (x=0.1, 0.15…)	Average reaction activation energy in α=x (kJ/mol)
ΔH	Enthalpy (kJ/mol)
ΔG	Gibbs free energy (kJ/mol)
ΔS	Entropy (kJ/mol)
R	Gas constant (kJ/(mol·K))
K_B	Boltzmann constant (kJ/K)
h	Plank constant (kJ/K)
T	Actual temperature (K)
$f(\alpha)$	Reaction mechanism function
β	Heating rate (K/min)
ΔTG_{Total}	Total weight loss of the whole process (%)
DTG_{max}	Maximum weight loss rate (%/℃)
T_{max}	Temperature at the maximum rate of weight loss (℃)
$\bar{T}_{max}$	Average temperature at the maximum weight loss rate (℃)
$\bar{T}_{\alpha=x}$ (x=0.1, 0.15…)	Average temperature in α=x (℃)
R^2	Goodness of Fit (-)
S	Standard deviation

Abbreviations

HT-CLSM	High-temperature confocal laser scanning microscopy
HT-SAOS	High-temperature small amplitude oscillatory shear
TG	Thermogravimetric
MS	Mass spectrometric
DTG	Derivative thermogravimetric
FWO	Flynn-Wall-Ozawa
KAS	Kissinger-Akahira-Sunose
I	Inertinite
V	Vitrinite
L	Liptinite
M	Mineral
IC-R	Raw imported coal
NC-R	Raw native coal
IC-V	Vitrinite from imported coal
IC-I	Inertinite from imported coal
NC-V	Vitrinite from native coal
NC-I	Inertinite from native coal
E	Expansion
S	Shrinkage
Avg	Average

1. Introduction

Coke, as a principal product in the process of coal dry distillation and upgrading [1], plays a pivotal role in blast furnace ironmaking [2][3]. For a developing country like China, where steel production has surged yearly over the past decades [4], the amount of coal consumed enormously is caused by the demand for metallurgical coke [5]. With the dramatically decreasing high-quality coal resources and the tightening energy policy [6], how to realize the efficient utilization of coal in the coking industry has become an outstanding issue of practical significance.

Petrologists have discovered that coal is composed of macerals which are vitrinite [7], inertinite [8], and liptinite [9]. Compared with the traditional procedure of guiding production by macroscopic coal properties, utilizing the intrinsic attributes of each component in coal to help the production of coal chemicals and other industries has become an effective way [10][11]. It is now well established from the rock type of macerals by relevant scholars that vitrinite and liptinite are thermally active and have natural advantages in energy conversion [12], while the low activity possessed by the inertinite gives it more potential for the preparation of functional materials [13]. Therefore, it is highly promising to explore the features of macerals based on coal petrology to specify the disparities in application peculiarities and thus facilitate coal utilization.

The specific pyrolysis behavior of coal during the coking process is precious in instructing the transformation of related products such as gas [14], tar [15], and coke [16]. The coking reactions [17][18], molecular transformations [19], and product behavior during the thermal evolution of coal are further elucidated in the context of current thermal characterization techniques in waste [20], biomass [21], and fossil fuel processing [22]. Among them, numerous reports have manifested that the caking property of coal makes a noteworthy contribution to the smoothness of coking process and the assurance of coke quality [23][24]. Furthermore, the adhesion of coal occurs mainly at 300-550 °C [25][26], in which the temperature interval is accompanied by the escape of volatile substances and the formation of metaplast with adhesive tendency [27][28], leading to the widely accepted opinion

that metaplast with transient plasticity produced by the thermal softening of coal is essential to determine the caking capacity [29][30]. Consequently, it is necessary to scrutinize this prominent period of coal.

By offline or online observation of morphology and structure of coal-based materials, previous studies have observed that their carbon ordering [31], expansion [32], and permeability during coking are mutable [33], with different degrees of variability for various coal types. It was further revealed by thermogravimetric analysis that the thermal stability of metaplast generated from different coals differed substantially [34], which combined with mass spectrometry uncovered that the aliphatic content endowed in the coal appeared to show a positive correlation with the persistence of the metaplast presence [35][36]. More in-depth research has shown that plentiful aliphatic structures are sequestered in vitrinite [37], hence the content of vitrinite is presumed to be the dominant factor in the modification of coke quality [38]. Nevertheless, few studies have been conducted to directly examine the thermogravimetric properties of macerals to ascertain the dominance of different coals into cokes. Concurrently, the above means is superior in refining the steps of chemical reactions from a trace perspective, but it is not convincing enough for analyzing the coal adhesive performance.

In recent years, the application of rheology to observe the rheological response of coal to catch more accurate viscoelasticity of metaplast has received much attention [39][40]. In contrast to the traditional coal caking indicators, rheological testing supported by dynamic mechanical analysis can directly characterize the viscosity of metaplast to capture quantitative flow-solidification information during coal-to-coke conversion [41][42][43], which can serve to examine the thermal changes of coal and the interaction between different substances [44][45]. Remarkably, there are few studies in the available literature on the genetic relationship of properties between raw coal and single maceral during pyrolysis. Although the effects of thermoplastic and thermal stability of raw coal on coking behavior have been considered, the sources of differences in fluid phases and their properties of different coal types have hardly been systematically explored, much less applied in organic

association with their adhesive reaction mechanisms. Accordingly, based on the perspective of raw coal concentrate combined with the existing advanced experimental equipment, can be regarded as an effective contribution to further understanding of the caking mechanisms in coal.

This study was to access the thermo-rheological behavior of metaplast produced by conventional coal types in the transient plasticity phase and the differences in the pyrolytic mechanism as well as to provide theoretical assistance to further clarify the coal caking property. The vitrinite and inertinite enrichments were collected by float-sink separation, and the mobility characteristics of different components were characterized online using high-temperature confocal laser scanning microscopy. Then the variations of complex viscosity, phase angle, and plate gap of coal and its macerals with temperature were measured by high-temperature small amplitude oscillatory shear rheometer. Additionally, the divergences in thermal stability and reaction process of different coals in the thermal plastic stage were analyzed by coupling of thermogravimetric-mass spectrometric. Eventually, the kinetics and thermodynamics of coal pyrolysis under various heating rates were calculated to elicit the reaction activation energy (E_α), enthalpy (ΔH), Gibbs free energy (ΔG), and entropy (ΔS).

2. Experimental

2.1 Sample preparation

The process flow diagram of this experiment is shown in **Fig. 1**, and two feedstocks used were raw imported coal (IC-R) and native coal (NC-R). The vitrinite (IC-V, NC-V) and inertinite enrichments (IC-I, NC-I) of the two coals were get separately by the hydrothermal float-sink method as shown in **Fig. 1(b)**, which was demonstrated systematically in our previous work [46]. The results of proximate, ultimate, and petrographic analyses of all samples are shown in **Table 1**, and it was found that IC and NC are coking coal and gas coal, respectively. Following the examination of the basic properties of each sample, it is essential to investigate their thermal properties, and the specific methodology used is shown in **Fig. 1(c)**.

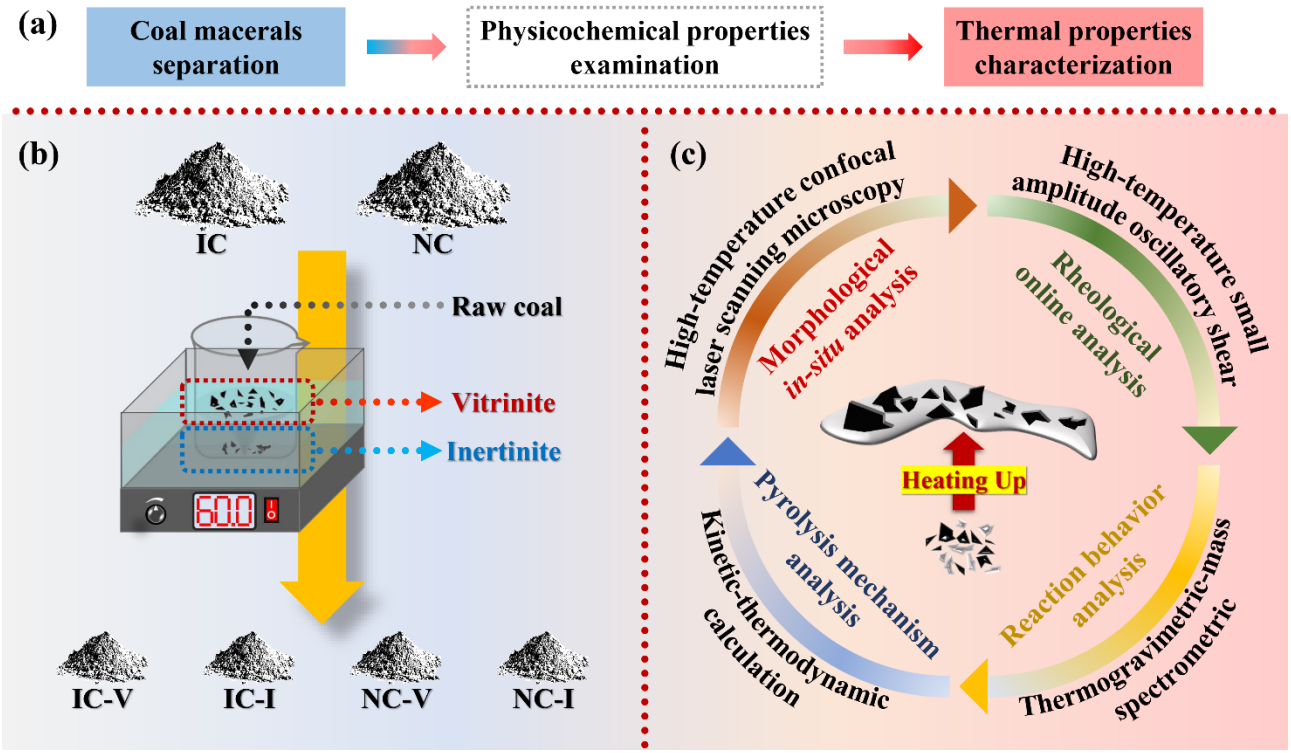

Fig. 1. Illustration of this experimental procedures: (a) process flow configuration; (b) coal maceral separation method; (c) thermal properties characterization method.

Table 1. Analysis of basic physicochemical properties of coal and its maceral enrichment [46].

Coal sample		IC-R	IC-V	IC-I	NC-R	NC-V	NC-I
Proximate analysis (%)	A^*_{ad}	7.870	5.520	8.230	7.780	5.450	8.470
	M_{ad}	1.620	1.760	1.230	1.310	2.040	1.120
	V_{ad}	19.29	23.68	15.46	39.56	33.87	21.16
	FC_{ad}	71.22	69.04	75.08	51.35	58.64	69.25
Ultimate analysis (%)	C_{ad}	81.11	81.27	79.83	77.10	78.66	74.85
	H_{ad}	4.930	4.560	3.790	5.170	4.460	3.930
	O_{ad}	2.550	4.950	5.280	6.460	7.330	9.780
	N_{ad}	1.500	1.480	1.170	1.700	1.510	1.290
	$S_{t,ad}$	0.4200	0.4600	0.4700	0.4800	0.5500	0.5600
Petrographic analysis (%)	I	21.39	16.86	64.62	22.01	8.020	72.00
	V	67.89	76.82	26.24	69.45	82.76	19.04
	L	3.820	4.290	2.020	2.500	5.050	2.740
	M	6.900	2.030	7.120	6.040	4.170	6.220
	$\bar{R}_{max}$	1.326	—	—	0.8400	—	—

A^*: ash; M: moisture; V: volatile; FC: fixed carbon; ad: air dry basis; t: total; I: inertinite; V: vitrinite; L: liptinite; M: mineral; $\bar{R}_{max}$: vitrinite reflectance

2.2 High-temperature confocal laser scanning microscopy analysis

The high-temperature confocal laser microscopy (HT-CLSM, VL2000DX-SVF17SP), which can withstand a maximum temperature of 1750 °C, was set up to visualize the soft-melting expansion behavior of coal-based samples online during the heating process. A few coal particles of 0.125-0.250 mm in diameter were dispersed in a corundum crucible (8.0 mm diameter×5.0 mm depth) lined with a nickel sheet to observe the flow-solidification of coal macerals *in-situ* by the light-dark contrast between crystalline nickel and amorphous carbon at high temperature. The vacuum operation of the facility was operated before the test, then 200 mL/min of nitrogen was consecutively passed to avoid the effect of oxidation and volatility on the field of view. The temperature was first increased from room temperature to 200 °C at a rate of 50 °C/min and held for 1 min, then continued to 1000 °C at a rate of 100 °C/min. The processing of the photo and data measurement was performed in ImageJ software.

2.3 High-temperature small amplitude oscillatory shear analysis

The high-temperature small amplitude oscillatory shear rheometer (HT-SAOS, MCR702MD) equipped with the PP25TS measurement system and CTD600 temperature control system was employed to examine the complex viscosity, phase angle, and plate gap response to the temperature of all samples. The 0.5 g powder sample was clamped between parallel plate rotors after setting the oscillation mode with an amplitude of 0.1%, frequency of 1 Hz, and applying a constant normal force of 5 N. The sample was heated from room temperature to 260 °C at a heating rate of 20 °C/min followed by a temperature scan in the interval of 260-550 °C with a heating rate of 5 °C/min. Nitrogen at 15 L/min was required throughout the test to protect the sample against oxidation.

2.4 Thermogravimetric and mass spectrometric analysis

2.4.1 Thermogravimetric and derivative thermogravimetry analysis

The thermal analyzer (PerkinElmer Pyris Diamond) was adopted for thermogravimetric (TG) and derivative thermogravimetric (DTG) analysis. A protective atmosphere with 100 mL/min of argon was introduced throughout the experiment. Each sample weighed 15±0.5 mg and was loaded

into a corundum crucible. All samples were heated from room temperature to 1000 °C at a heating rate of 5 °C/min, 10 °C/min, and 20 °C/min, respectively. The change in the weight of each sample over time was recorded during each experiment.

2.4.2 Mass spectrometric analysis

The gas mass spectrometer (MS, Pfeiffer Vacuum OmniStar) with a detection limit <1 ppm is connected to the thermal analyzer via a stainless-steel capillary tube. The mass/charge ratios (*m/z*) were in the range of 1-300 amu with a scan rate of 500 ms/amu, detection focused on the precipitation behavior of water (H_2O, *m/z*=18), carbon dioxide (CO_2, *m/z*=44), hydrogen (H_2, *m/z*=2), methane (CH_4, *m/z*=16), sulfur dioxide (SO_2, *m/z*=64), and thiophene (C_4H_4S, *m/z*=84) because of the complex chemical structure of coal consisting mostly of C, H, O and the important influence of S migration on subsequent metallurgical processes.

2.5 Kinetic and thermodynamic analysis

2.5.1 Kinetic parameters analysis

The kinetics of non-isothermal pyrolysis of coal conforms to the Arrhenius equation as shown in **Eq. (1)** [47]:

$$\frac{\mathrm{d}\alpha}{\mathrm{d}t} = A\exp\left(-\frac{E_\alpha}{RT}\right)f(\alpha) \tag{1}$$

where, α ($\alpha = \frac{m_0 - m_t}{m_0 - m_\infty}$) is the conversion rate; m_0 is the initial mass of the substance (mg); m_t is the mass of the substance at moment *t* (mg); m_∞ is the mass of the pyrolysis end-temperature residue (mg); A is the pre-exponential factor (1/min); E_α is the reaction activation energy of the substance (kJ/mol); the gas constant is R=8.314×10^{-3} (kJ/(mol·K)); T is the actual temperature (K); $f(\alpha)$ is the reaction mechanism function.

β is the heating rate (K/min) with the mathematical expression shown in **Eq. (2)**:

$$\beta = \frac{\mathrm{d}T}{\mathrm{d}t} \tag{2}$$

Substituting **Eq. (2)** into **Eq. (1)** results in the kinetic equation for the pyrolysis reaction as

shown in **Eq. (3)** [48]:

$$\frac{\mathrm{d}\alpha}{\mathrm{d}T} = \frac{A}{\beta}\exp\left(-\frac{E_\alpha}{RT}\right) f(\alpha) \tag{3}$$

Integration of **Eq. (3)** results in the integral form as **Eq. (4)**:

$$g(\alpha) = \int_0^\alpha \frac{\mathrm{d}\alpha}{f(\alpha)} = \frac{A}{\beta}\int_0^T \exp\left(-\frac{E_\alpha}{RT}\right)\mathrm{d}T \tag{4}$$

Since the difficulty of determining $f(\alpha)$, it can be avoided the error caused by the variation of kinetic models to solve for E_α through iso-conversional (model-free) methods. In this work, the Flynn-Wall-Ozawa (FWO) and Kissinger-Akahira-Sunose (KAS) methods with relatively high reliability were chosen to arrive at E_α and *A* from the slope and intercept relationship [49]. Their mathematical expressions by approximate derivations are shown in **Eq. (5)** and **Eq. (6)** [50][51], respectively:

$$\ln\beta = \ln\frac{AE_\alpha}{Rg(\alpha)} - 5.331 - 1.052\left(\frac{E_\alpha}{RT}\right) \tag{5}$$

$$\ln\frac{\beta}{T^2} = \ln\frac{AR}{E_a g(\alpha)} - \frac{E_\alpha}{RT} \tag{6}$$

2.5.2 Thermodynamic parameters analysis

Based on the clarity of E_α and *A*, the ΔH (kJ/mol), ΔG (kJ/mol) and ΔS (kJ/mol) of chemical reactions can be further analyzed by **Eq. (7)-(9)** [49][52]:

$$\Delta H = E_\alpha - RT \tag{7}$$

$$\Delta G = E_\alpha + RT\ln\left(\frac{K_\mathrm{B}T}{hA}\right) \tag{8}$$

$$\Delta S = \frac{\Delta H - \Delta G}{T} \tag{9}$$

where, the Boltzmann constant is K_B=1.381×10^{-26} (kJ/K); the Plank constant is h=3.976×10^{-35} (kJ/min).

3. Results and discussion

3.1 Morphological changes of coal and its macerals during heating

The morphological changes of different coal-based samples attained by HT-CLSM online observation during the heating process are shown in **Fig. 2**, where 550 ℃ and 1000 ℃ stand for the plastic termination and the experimental end temperature of coal, and the rest of the temperatures shown are approximately representatives of the temperature at which deformation is imminent. In the field of view, we can identify all coals' expansion, flow-bonding, and shrinkage-solidification behavior. As shown in **Fig. 2(a)** and **(d)**, raw coal particles exhibit mutual adhesion after expanding and precipitating the adhesive phase. This tendency in both coals will be destroyed as the temperature increases to the shrinkage stage. The inertinite is essentially immutable, except for the sudden jump in IC-I at 750.2-817.0 ℃ shown in **Fig. 2(c)**, which is presumed to be caused by the pressure change in the equipment.

It is significant to mention that vitrinite shows fantastic flow and swelling features than raw coal and inertinite, however, there are naked-eye discriminations in the particular behavior of these two vitrinites. First of all, it is apparent from **Fig. 2(b)** that IC-V presents a marked multistage expanding-shrinking property and the particle becomes well-rounded after expansion by surface tension, which implies that the generation of metaplast occurs several times throughout the plasticity interval of IC-V and the fluidity of this material is excellent. On the contrary, the NC-V in **Fig. 2(e)** has only a single expansion, and the amount of metaplast generation is low enough to maintain the earliest morphological characteristics. Alternatively, the expansion temperatures of the two vitrinites also differ drastically. IC-V undergoes a sharp change in expansion from 371.8 ℃ and continues to about 550.7 ℃, while NC-V begins to expand at 284.6 ℃ and slowly continues to 416.8 ℃. Even though NC-V from low-rank gas coal starts softening at a lower temperature, its expansion temperature interval is shorter than that of IC-V from high-rank coking coal.

Fig. 2. Morphological changes of two coal types and their macerals during *in-situ* heating, where the letters "E" and "S" represent "expansion" and "shrinkage", respectively: (a) IC-R; (b) IC-V; (c) IC-I; (d) NC-R; (e) NC-V; (f) NC-I.

Further semi-quantitative analysis of the expansion relationship between vitrinite and inertinite of two coal types was performed. The specific expansion parameters calculated based on the area of the characteristic single particle samples (marked with red circles in **Fig. 2**) at different temperatures are shown in **Fig. 3**. It can be noticeably found that the former two expansion-shrinkage behaviors of IC-V in the thermoplastic process are the most prominent, and both of their expansion rates exceed 80%, while the maximum expansion rate of NC-V is only 12.41%. However, the lowest expansion rate is found in inertinite of both raw coals, which is only about 1.5%. Obviously, the flow-adhesive

potential of the four macerals can be ordered according to the expansion degree as IC-V>NC-V>IC-I>NC-I. Not only the expansion characteristic of vitrinite is outperformed by inertinite, but also the vitrinite of gas coal has better flow behavior than the inertinite of coking coal, which is meaningful to improve the possibility of coking with poor-grade coal ratio by controlling the raw coal concentrate.

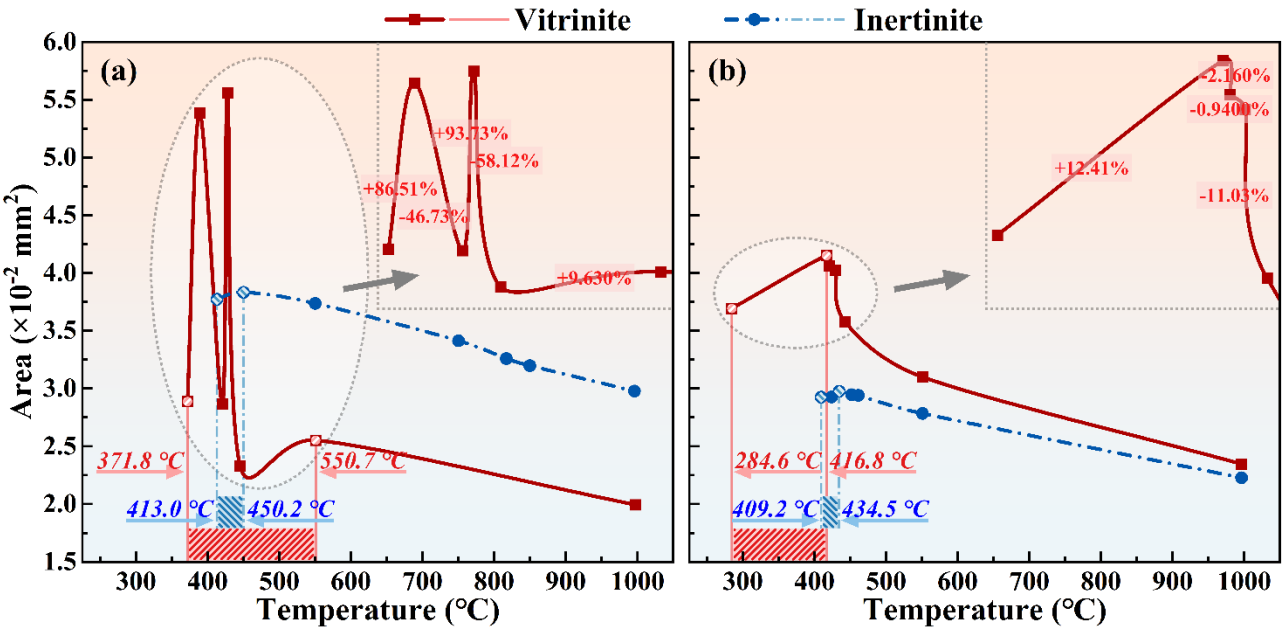

Fig. 3. Area of macerals from two coal types at characteristic temperatures: (a) IC; (b) NC.

3.2 Viscoelastic differences of coal and its macerals during pyrolysis

The thermo-rheological properties of raw coal and its macerals shown in **Fig. 4** help us to understand more thoroughly the softening behavior of coal. It is evident that all coal-based materials achieve synergistic changes in fluidity and expansion in the range of 350-500 °C, but different samples have distinct characteristics belonging to each individual.

The significant change in complex viscosity, which can directly characterize the fluidity of materials, has attracted much attention. Firstly, an impressive finding comes from **Fig. 4(b)** and **(e)**, where the minimum composite viscosity point "P" exists for IC-V (462.9 °C, 1.812×10^5 Pa·s) and NC-V (408.1 °C, 0.6551×10^5 Pa·s) represented by vitrinite, which further confirms that it is the key supplier of softened mobile phase in raw coal. Secondly, notwithstanding the absence of a decreasing

viscosity trend for the raw coals tested, there is a temperature interval in which they maintain a steady state. Among them, the same result has been found in the HT-CLSM test that NC-R has an earlier metaplast generation temperature compared to IC-R, but its poor heat resistance leads to rapid decomposition. It is noticeable that the viscosity increase of NC-V and IC-V starts respectively at 270.4°C and 390.6°C, thus indicating a parallel relationship between the softening behavior of different raw coals and their vitrinite. Coupled with the results of HT-CLSM, it stands to reason that metaplast formation and decomposed solidification are coexisting in the diagonally shaded region of the figure. Lastly, the inertinite of both coals does not exhibit flowable characteristics in terms of complex viscosity.

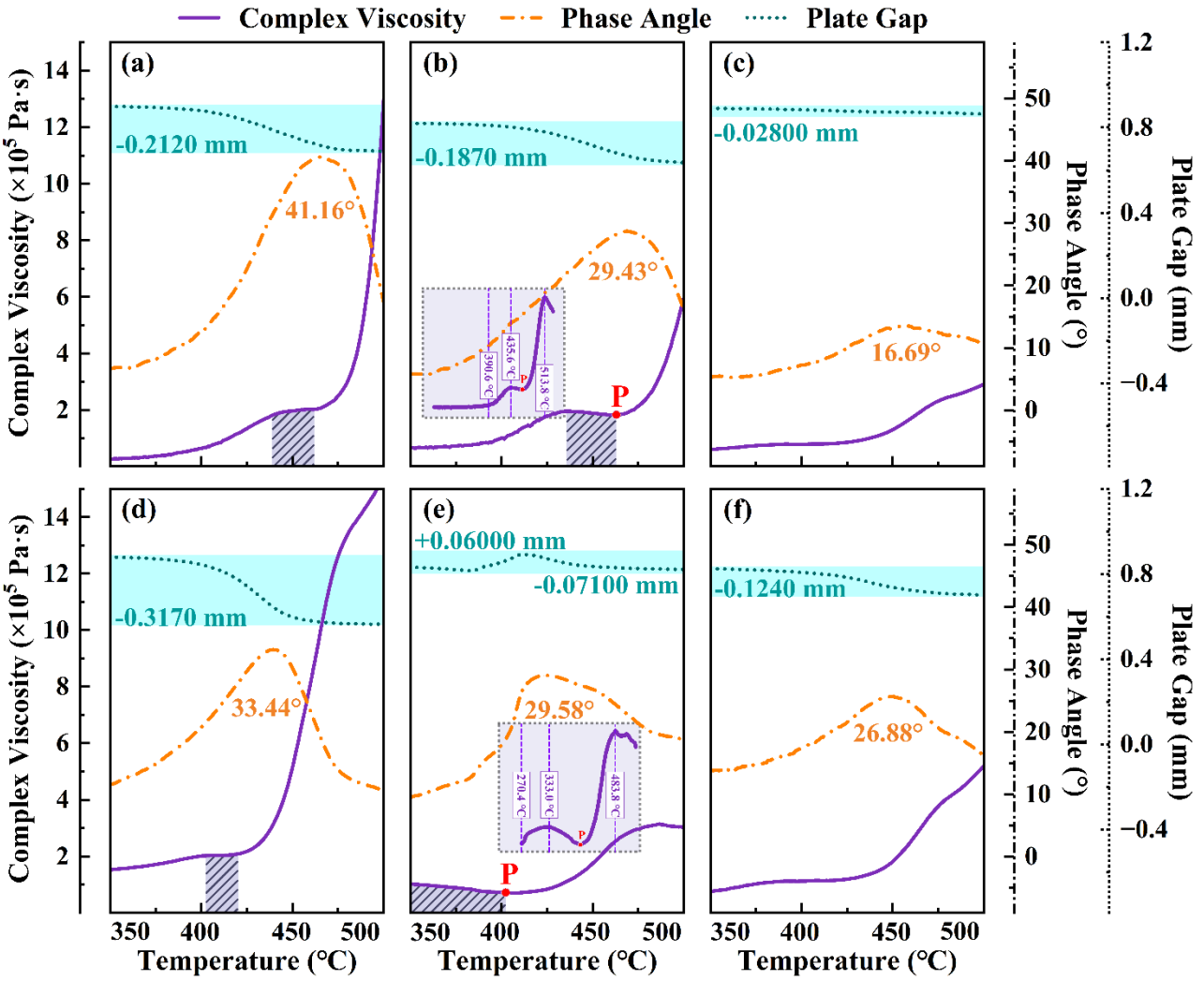

Fig. 4. Rheological properties of all samples, where point "P" is the minimum value of the complex viscosity: (a) IC-R; (b) IC-V; (c) IC-I; (d) NC-R; (e) NC-V; (f) NC-I.

Another interesting finding is the maximum complex viscosity throughout the heating process, which reaches 8.097×10^5 Pa·s at 513.8 °C for IC-V and 3.175×10^5 Pa·s at 483.8 °C for NC-V. Since the complex viscosity is proportional to the complex modulus (the sum of the storage and loss moduli) and the complex modulus of the solid is mainly contributed by the storage modulus, follows that IC-V has higher elastic solid characteristics than NC-V after curing. Combined with the expansion of the two raw coals, there is a clear indication that the IC produces a cohesive material that exceeds the NC in terms of fluidity and consolidation force.

From the perspective that the phase angle is positively correlated with the mobility, we can see that all samples have the law of raw coal>vitrinite>inertinite. Nevertheless, except for the relatively more protrusive phase angle of IC-R, the phase angles of the rest are less than 35°, which proves that they still behave mainly as solid or gel-like [19]. Finally, as can be seen from the plate gap variation, the exception is NC-V was detected for expansiveness, with most of the samples contracting slowly in this 150 °C interval. Considering the own properties of both coals and the experimental results, it is concluded that the samples belonging to the NC group of gas coals have superiority under the closed swelling test due to their powerful gas production competence. Whereas in the coking performance, the quality of the metaplast produced by IC-V in coking coal is more favorable.

3.3 Thermogravimetric variations of coal and its macerals

The reason for the distinctions in coal mobility is next explained in terms of the thermogravimetric behavior of coals and their macerals. As shown in **Fig. 5**, it can be found that the DTG curves of all samples contain three weight loss peaks, which are two inconspicuous peaks at low temperature (①) and high temperature (②) in the site of local amplification, and one exceedingly obvious medium temperature reaction peak. Therefore, the thermal behavior of raw coal and its corresponding components can be roughly divided into three stages, where *Stage 1*: the release of water and its physically bound small molecules in solids mainly in the period below 200 °C, and the breakage of weak bonds in the samples; *Stage 2*: the intense weight loss reaction interval in the range

of 200-700 °C, this main weight loss process is coupled by chemical changes such as the cleavage and precipitation of volatile covalently bonded macromolecules represented by gas-tar and the cleavage reaction of residual materials [53]; *Stage 3*: the slow decomposition reaction of authigenic minerals and carbon condensation reactions of coal above 700 °C [54]. Although the increase in heating rate will lead to the thermal hysteresis of the TG-DTG curve, it has no decisive influence on the pyrolysis reaction stage.

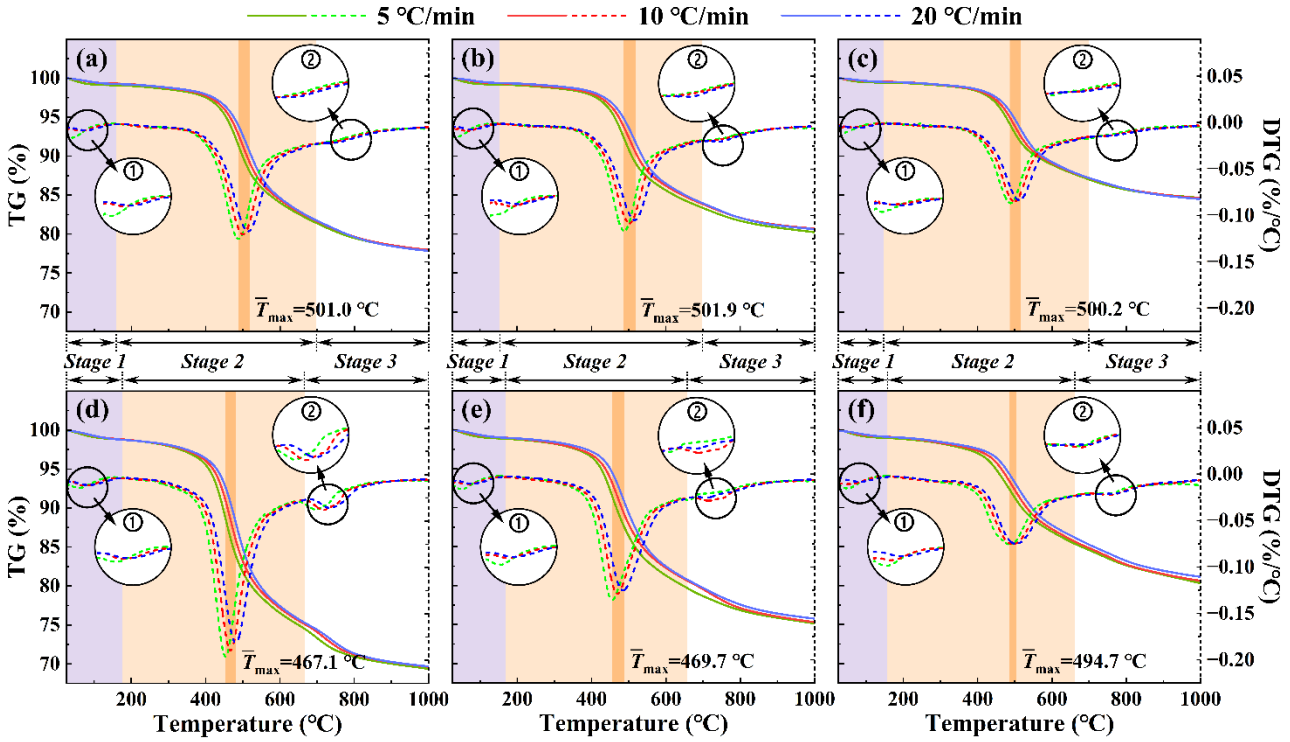

Fig. 5. TG-DTG variations of all samples at different heating rates, $\overline{T}_{max}$ represents the average temperature at the maximum weight loss rate of the three heating rates: (a) IC-R; (b) IC-V; (c) IC-I; (d)NC-R; (e)NC-V; (f) NC-I.

The pyrolysis characteristic parameters of each sample after further analysis are shown in **Table 2**. For the weight loss sensitivity of the reactants, there is an order of raw coal>vitrinite>inertinite in terms of weight loss rate and final weight loss, and the rule of vitrinite>raw coal>inertinite is maintained for the maximum weight loss temperature and thermal hysteresis. According to previous studies, the simultaneous pyrolysis of vitrinite and inertinite will interact [44][45], which may enable better catalytic devolatilization of raw coal. Nonetheless, the same coal-based samples from distinct

species have their peculiarities in pyrolysis. For example, the weight loss capacity of all NC group samples is stronger than that of the IC group followed by the width of the orange interval in the figure and DTG_{max}, which shows that NC group samples have lower thermal hysteresis due to a significant maximum weight loss rate compared to IC group samples. All these imply that the NC group has superior thermal reactivity circumstances can be explained by the high volatile content of gas coal and the mature and stable properties of coking coal.

Table 2. Characteristic parameters of thermal weight loss of coal samples.

Sample	Heating rate (℃/min)	$\triangle TG_{Total}$ (%)	DTG_{max} (%/℃)	T_{max} (℃)
IC-R	5	22.12	-0.1251	489.1
	10	22.03	-0.1203	500.2
	20	22.17	-0.1171	513.7
IC-V	5	19.77	-0.1166	487.3
	10	19.31	-0.1086	502.3
	20	19.38	-0.1049	516.0
IC-I	5	15.36	-0.08668	489.0
	10	15.39	-0.08508	498.7
	20	15.51	-0.08336	513.0
NC-R	5	30.63	-0.1960	453.4
	10	30.37	-0.1895	467.0
	20	30.32	-0.1812	481.0
NC-V	5	24.86	-0.1359	455.0
	10	24.68	-0.1287	469.3
	20	24.24	-0.1252	484.7
NC-I	5	19.70	-0.07574	486.8
	10	19.37	-0.07531	494.5
	20	18.87	-0.07500	502.7

$\triangle TG_{Total}$: total weight loss of the whole process; DTG_{max}: maximum weight loss rate; T_{max}: temperature at the maximum rate of weight loss.

In addition, as the most dominant reaction stage in the pyrolysis process, the *Stage 2* interval of NC and its macerals is significantly shorter than that of IC, which is corresponding well to the softening persistence behavior of both coals. *Stage 1* and *Stage 3*, represented by dehydration and thermal decomposition of minerals, are more persistent. It is puzzling that the moisture and ash contents gained from the proximate analysis of raw materials are contrary to this conclusion. However, it is worth noting that the mineral decomposition peak in the figure is most pronounced in raw coal, followed by vitrinite, and weakest in inertinite. This phenomenon indicates that the catalytic

effect of minerals on the active component is more obvious, which in turn explains the reason for the above results.

Fig. 6 reflects the product precipitation performance of two raw coals and their macerals under different heating conditions. Overall, it seems that the volatilization of gaseous products has a good correspondence with the thermogravimetric behavior. Although there is also a thermal lag in the reception of the mass spectrometry signal as the heating rate increases, rapid heating has a facilitating effect on the release of volatiles in raw material.

Among the six gas products, H_2O and CO_2 exhibit distinct multi-stage generation properties, whether from raw coal or macerals. During the period from room temperature to 300 °C, it contains the disengage of surface water, bound water, and crystal water of clay minerals in coal. Because of the different types of oxygen-containing functional groups, the dehydration condensation reaction after bond breaking was carried out at 400-620 °C and higher than 620 °C, respectively, and the latter released more H_2O [37]. The main production intervals of CO_2 are in the range of 400-620 °C and 620-850 °C, which fully exemplifies that CO_2 comes from the thermal decomposition of more stable oxygen-containing heterocycles and carbonates [50]. Significantly, these two innocuous emissions are almost exclusively produced in the high-temperature region and vitrinite shows a greater gas production capacity than inertinite, which points to a large number of reactive functional groups in vitrinite that are easily destroyed.

Furthermore, the evolution of H_2 and CH_4 during pyrolysis can be available in **Fig. 6(b)**, **(e)**, and **(h)**. The massive yield intervals of these two gases are more concentrated, both of which are formed after 400 °C, and the vitrinite of two coals displays stronger volatilization potential than inertinite. Surprisingly, the H_2 manufacture behavior of IC-R is extremely prominent, even exceeding the vitrinite of IC, again due to the coupling effect of vitrinite, inertinite, and minerals in raw coal. Simultaneously, IC has a stronger ability to produce flammable gas than NC, which proves that high-rank coal is rich in more aliphatic substances.

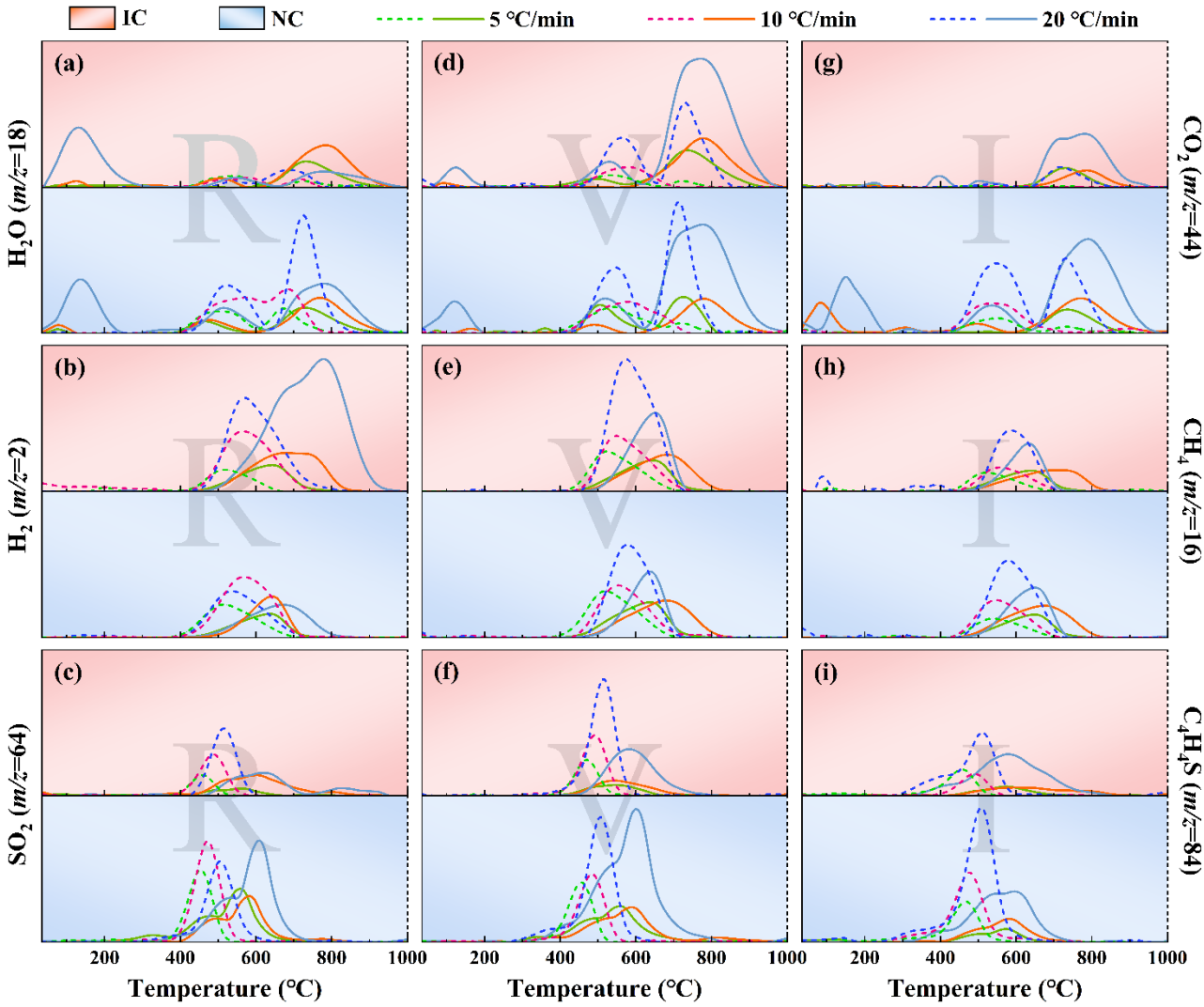

Fig. 6. Behavior of two coals releasing six characteristic substances at three heating rates: (a) Release of H_2O and CO_2 in raw coal; (b) Release of H_2 and CH_4 in raw coal; (c) Release of SO_2 and C_4H_4S in raw coal; (d) Release of H_2O and CO_2 in vitrinite; (e) Release of H_2 and CH_4 in vitrinite; (f) Release of SO_2 and C_4H_4S in vitrinite; (g) Release of H_2O and CO_2 in inertinite; (h) Release of H_2 and CH_4 in inertinite; (i) Release of SO_2 and C_4H_4S in inertinite.

It is interesting that the blowdown intervals for sulfur-containing pollutants during coal pyrolysis are distinctly wider than those for H_2 and CH_4, and SO_2 is produced at higher temperatures but in lower yields than C_4H_4S. Remarkably, the three samples of NC have more sulfur-containing products generated compared to IC, which can be associated with the ultimate analysis and evidence of the easier reaction of sulfur-containing bonds in gas coal. Besides, the C_4H_4S produced by vitrinite and

inertinite behaves similarly in NC, but SO_2 is produced more in vitrinite. It is possible to speculate that the generation mechanism of these two sulfur-containing compounds is different, which can also indicate that vitrinite is richer in the oxygen-containing functional group than inertinite.

Considering the TG-DTG results, it may be safely said that the largest thermal weight loss rate of *Stage 2* is attributed to the superposition of individual chemical reactions in this temperature interval. Vitrinite in all raw coals has a more distinguished thermal activity, and the younger gas coals have a greater weight loss rate. This is also in line with the previous section that NC-V is easy to soften but difficult to persist. Concurrently, according to the mass spectra, H_2O and sulfur-containing gases predominate among the main products of the lower-rank coal, with less pyrolytic H_2 and CH_4 from aliphatic structures. Thereby, despite being the active component in coal, the relevant thermal properties of vitrinite vary considerably among coal types. These differences mainly originate from the chemical nature of different coals and their macerals, which suggests that the structures of different macerals need to be investigated in more depth in the future.

3.4 Kinetic and thermodynamic mechanisms of coal and its macerals

To characterize the thermal conversion behavior of the coal-based samples comprehensively, we evaluated their pyrolysis activation energy (E_α) and pre-exponential factor (A). The visualization models of the parameters accomplished using the two methods are shown in **Fig. 7**, it should be noted that this experiment aims to solve the expanding-caking law of coal, so the selected conversion range is α=0.1-0.6, which covers the softening interval of coal.

The values of kinetic parameters are listed in **Table 3**, it is reasonable to consider this calculation of fitting accuracy on the basis of R^2 since its values are almost greater than 0.9. E_α in the reaction interval is (1) IC-R: 283.0 kJ/mol (FWO), 285.1 kJ/mol (KAS); (2) IC-V: 270.3 kJ/mol (FWO), 271.7 kJ/mol (KAS); (3) IC-I: 300.5 kJ/mol (FWO), 303.5 kJ/mol (KAS); (4) NC-R: 258.6 kJ/mol (FWO), 259.9 kJ/mol (KAS); (5) NC-V: 240.9 kJ/mol (FWO), 241.1 kJ/mol (KAS); (6) NC-I: 298.7 kJ/mol (FWO), 301.8 kJ/mol (KAS). Obviously, E_α followed the pattern of inertinite>raw coal>vitrinite in

both IC and NC groups, meaning that vitrinite has a lower reaction energy barrier than inertinite. However, uncertainty analysis reveals that inertinite occupies respectively the minimum (IC-I) and maximum (NC-I) values of S in the two groups of samples, and the E_α fluctuations in the samples of IC group are much smaller than those of NC group. Therefore, it is inferable that the difference in pyrolysis variation between vitrinite and inertinite in gas coal is much stronger than that in coking coal. As the empirical criterion of A>10^9 1/s can account for the composite and efficient reactivity of the reaction process [52], all samples satisfy this property. Meanwhile, A is a bridge to construct thermodynamic and kinetic calculations, which will not be interpreted extensively here.

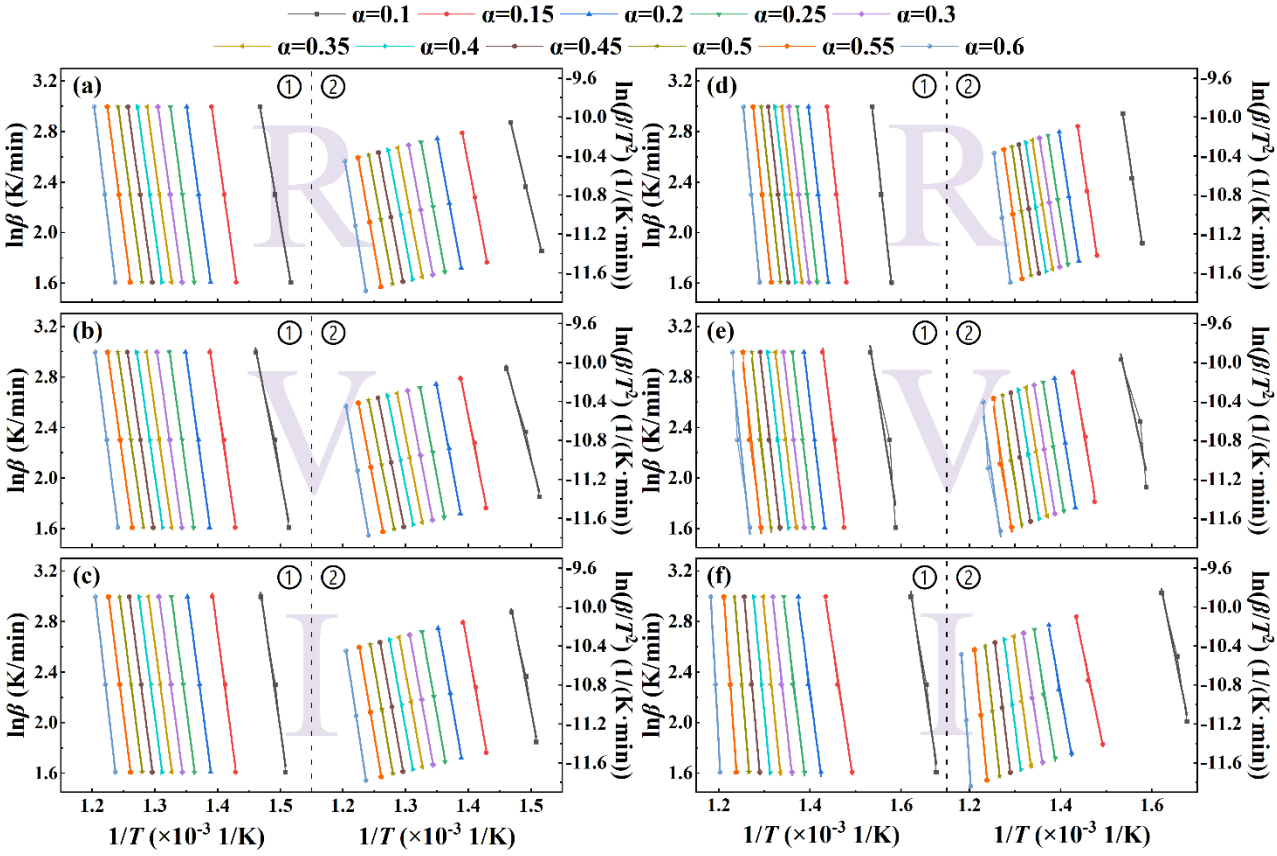

Fig. 7. Linear fit plots of kinetic parameters were obtained for various coal-based feedstocks by two methods, where ① and ② represent FWO and KAS, respectively: (a) IC-R; (b) IC-V; (c) IC-I; (d) NC-R; (e) NC-V; (f) NC-I.

Table 3 Kinetic parameters and fitting accuracy of all samples obtained by FWO and KAS methods.

Sample	Model	Parameter	α (-)											Avg	*S*
			0.1	0.15	0.2	0.25	0.3	0.35	0.4	0.45	0.5	0.55	0.6		
IC-R	FWO	E_α (kJ/mol)	223.2	276.3	286.1	286.6	284.5	282.0	280.9	281.9	286.2	298.4	326.7	283.0	24.10
		A (1/min)	1.536×10^{17}	1.614×10^{20}	2.052×10^{20}	8.752×10^{19}	2.988×10^{19}	1.099×10^{19}	5.325×10^{18}	3.595×10^{18}	4.016×10^{18}	1.369×10^{19}	4.176×10^{20}	8.540×10^{19}	1.309×10^{20}
		R^2 (-)	0.9993	0.9998	1.000	1.000	0.9999	0.9999	0.9999	0.9999	0.9999	0.9999	1.000	—	—
	KAS	E_α (kJ/mol)	223.7	279.0	288.9	289.2	286.7	284.0	282.7	283.5	287.9	300.6	330.0	285.1	24.75
		A (1/min)	1.618×10^{17}	2.343×10^{20}	3.012×10^{20}	1.240×10^{20}	4.045×10^{19}	1.424×10^{19}	6.680×10^{18}	4.432×10^{18}	4.979×10^{18}	1.795×10^{19}	6.346×10^{20}	1.257×10^{20}	1.980×10^{20}
		R^2 (-)	0.9992	0.9998	0.9999	0.9999	0.9999	0.9999	0.9999	0.9999	0.9999	0.9999	1.000	—	—
IC-V	FWO	E_α (kJ/mol)	204.9	269.2	283.4	282.3	276.7	271.3	268.1	267.1	269.4	278.6	302.6	270.3	24.01
		A (1/min)	4.800×10^{15}	4.346×10^{19}	1.238×10^{20}	4.133×10^{19}	8.133×10^{18}	1.928×10^{18}	6.771×10^{17}	3.534×10^{17}	3.010×10^{17}	6.932×10^{17}	1.217×10^{19}	2.117×10^{19}	3.771×10^{19}
		R^2 (-)	0.9897	0.9954	0.9978	0.9987	0.9993	0.9996	0.9998	0.9999	0.9999	0.9998	0.9992	—	—
	KAS	E_α (kJ/mol)	204.3	271.3	286.0	284.6	278.5	272.7	269.1	268.0	270.2	279.8	304.7	271.7	24.76
		A (1/min)	4.203×10^{15}	5.954×10^{19}	1.778×10^{20}	5.667×10^{19}	1.038×10^{19}	2.306×10^{18}	7.714×10^{17}	3.904×10^{17}	3.301×10^{17}	7.920×10^{17}	1.589×10^{19}	2.953×10^{19}	5.398×10^{19}
		R^2 (-)	0.9885	0.9950	0.9975	0.9985	0.9992	0.9996	0.9998	0.9998	0.9999	0.9998	0.9995	—	—
IC-I	FWO	E_α (kJ/mol)	272.8	296.4	295.6	295.4	295.2	295.1	295.7	297.8	302.9	315.6	343.1	300.5	17.23
		A (1/min)	1.357×10^{21}	5.502×10^{21}	1.078×10^{21}	3.915×10^{20}	1.834×10^{20}	9.517×10^{19}	5.917×10^{19}	4.706×10^{19}	5.680×10^{19}	2.009×10^{20}	5.242×10^{21}	1.292×10^{21}	2.065×10^{21}
		R^2 (-)	0.9895	0.9892	0.9981	0.9993	0.9991	0.9988	0.9993	0.9993	0.9995	0.9998	0.9999	—	—
	KAS	E_α (kJ/mol)	275.8	300.0	298.9	298.3	298.0	297.7	298.2	300.3	305.4	318.6	347.3	303.5	17.56
		A (1/min)	2.142×10^{21}	9.207×10^{21}	1.694×10^{21}	5.907×10^{20}	2.683×10^{20}	1.355×10^{20}	8.255×10^{19}	6.504×10^{19}	7.920×10^{19}	2.958×10^{20}	8.823×10^{21}	2.126×10^{21}	3.477×10^{21}
		R^2 (-)	0.9886	0.9942	0.9990	0.9996	0.9995	0.9993	0.9992	0.9993	0.9995	0.9998	0.9999	—	—
NC-R	FWO	E_α (kJ/mol)	260.2	257.1	253.0	249.7	247.5	246.4	246.8	250.0	258.2	274.4	301.6	258.6	16.43
		A (1/min)	1.226×10^{21}	2.665×10^{19}	3.530×10^{18}	9.200×10^{17}	3.552×10^{17}	1.794×10^{17}	1.218×10^{17}	1.294×10^{17}	2.939×10^{17}	2.124×10^{18}	6.746×10^{19}	1.207×10^{20}	3.672×10^{20}
		R^2 (-)	0.9973	0.9989	0.9993	0.9996	0.9998	0.9999	0.9999	1.000	1.000	0.9999	0.9991	—	—
	KAS	E_α (kJ/mol)	263.1	259.0	254.4	250.7	248.3	247.0	247.3	250.5	259.0	275.8	304.2	259.9	17.00
		A (1/min)	1.931×10^{21}	3.577×10^{19}	4.331×10^{18}	1.061×10^{18}	3.913×10^{17}	1.913×10^{17}	1.274×10^{17}	1.358×10^{17}	3.214×10^{17}	2.555×10^{18}	9.486×10^{19}	1.882×10^{20}	5.787×10^{20}
		R^2 (-)	0.9971	0.9988	0.9993	0.9996	0.9998	0.9999	0.9999	1.000	1.000	0.9999	0.9991	—	—
NC-V	FWO	E_α (kJ/mol)	178.6	229.7	240.7	240.9	239.9	240.1	243.1	249.1	257.1	264.1	266.2	240.9	23.49
		A (1/min)	2.185×10^{14}	1.625×10^{17}	3.180×10^{17}	1.499×10^{17}	6.930×10^{16}	4.198×10^{16}	4.067×10^{16}	6.259×10^{16}	1.217×10^{17}	1.810×10^{17}	1.099×10^{17}	1.143×10^{17}	8.829×10^{16}
		R^2 (-)	0.9093	0.9912	0.9998	0.9998	0.9993	0.9988	0.9981	0.9959	0.9895	0.9725	0.9325	—	—
	KAS	E_α (kJ/mol)	177.2	230.2	241.5	241.4	240.2	240.2	243.2	249.4	257.6	264.7	266.7	241.1	24.01
		A (1/min)	1.590×10^{14}	1.712×10^{17}	3.477×10^{17}	1.583×10^{17}	7.044×10^{16}	4.164×10^{16}	4.031×10^{16}	6.349×10^{16}	1.279×10^{17}	1.945×10^{17}	1.155×10^{17}	1.210×10^{17}	9.699×10^{16}
		R^2 (-)	0.8990	0.9903	0.9998	0.9998	0.9992	0.9987	0.9979	0.9955	0.9885	0.9698	0.9262	—	—
NC-I	FWO	E_α (kJ/mol)	192.5	187.4	218.3	238.8	261.1	284.8	304.7	322.8	348.2	400.4	527.1	298.7	100.4
		A (1/min)	2.602×10^{16}	1.065×10^{14}	4.760×10^{15}	5.772×10^{16}	1.059×10^{18}	2.325×10^{19}	2.604×10^{20}	1.993×10^{21}	4.153×10^{22}	3.805×10^{25}	1.136×10^{33}	1.032×10^{32}	3.424×10^{32}
		R^2 (-)	0.9827	0.9969	0.9927	0.9930	0.9946	0.9959	0.9970	0.9982	0.9994	1.000	0.9992	—	—
	KAS	E_α (kJ/mol)	192.4	185.8	217.8	239.0	262.3	286.9	307.7	326.5	353.0	407.6	540.6	301.8	104.7
		A (1/min)	2.479×10^{16}	7.532×10^{13}	4.119×10^{15}	5.823×10^{16}	1.233×10^{18}	3.119×10^{19}	3.876×10^{20}	3.225×10^{21}	7.563×10^{22}	8.823×10^{25}	4.357×10^{33}	3.961×10^{32}	1.314×10^{33}
		R^2 (-)	0.9808	0.9966	0.9920	0.9923	0.9941	0.9956	0.9968	0.9981	0.9994	1.000	0.9910	—	—

Avg: average; R^2: goodness of fit; *S*: standard deviation.

In particular, although there are fewer previous studies on the kinetics of pyrolysis of coal macerals, we believe it is still necessary to consider the differences between the existing and presently obtained pyrolytic activation energies of raw coals. **Table 4** shows the activation energies of pyrolysis obtained by the KAS and FWO methods for coals with volatile contents in the range of 17.38-48.73% in the interval of α=0.1-0.6. It can be seen that the standard deviation of E_α using the KAS and FWO method are kept at the single-digit level and below, except for Ningdong coal. Therefore, both methods apply to the samples of interest in this work. Meanwhile, the E_α of IC-R and NC-R are similar to those of published Yiluo coal and Inner Mongolia coal, respectively, where the volatile fraction of IC-R and Yiluo coal are comparable. The volatile fraction contents of all samples are inconsistent, but the present calculation can still be regarded as credible considering the differences in sample, experimental equipment, and environment.

Table 4 Comparison of the average value of E_α in α=0.1-0.6 from reported work.

Coal sample	References	$\bar{E}_{\alpha=0.1-0.6}$ (kJ/mol)		
		FWO	KAS	*S*
Powder River Basin coal	[47]	211.1	210.8	0.2121
Yiluo coal	[48]	277.5	275.6	1.344
Ningdong coal	[51]	214.8	232.8	12.73
A coal	[55]	237.4	227.5	7.000
Inner Mongolia coal	[56]	258.3	252.2	4.313
NC-R	This work	258.6	259.9	0.9192
IC-R	This work	283.0	285.1	1.485

$\bar{E}_{\alpha=0.1-0.6}$: average reaction activation energy in α=0.1-0.6; *S*: standard deviation.

The relationship between coal pyrolysis mechanism and physicochemical properties can be further optimized by examining the progression of E_α under the reaction progress from **Fig. 8**. There is an increasing-decreasing-increasing trend of E_α for IC-R, while NC-R directly decreases and then increases, suggesting that the pyrolysis mechanisms of the two coals are contrastive. In the presented results it is demonstrated that the E_α alteration behavior of IC-V and IC-R is extraordinarily similar. The behavior of NC-V is not only the opposite of NC-R but different from IC-V as well. For example,

the E_α of NC-V tends to be flat at α=0.2, while IC-V starts to decrease at the same time.

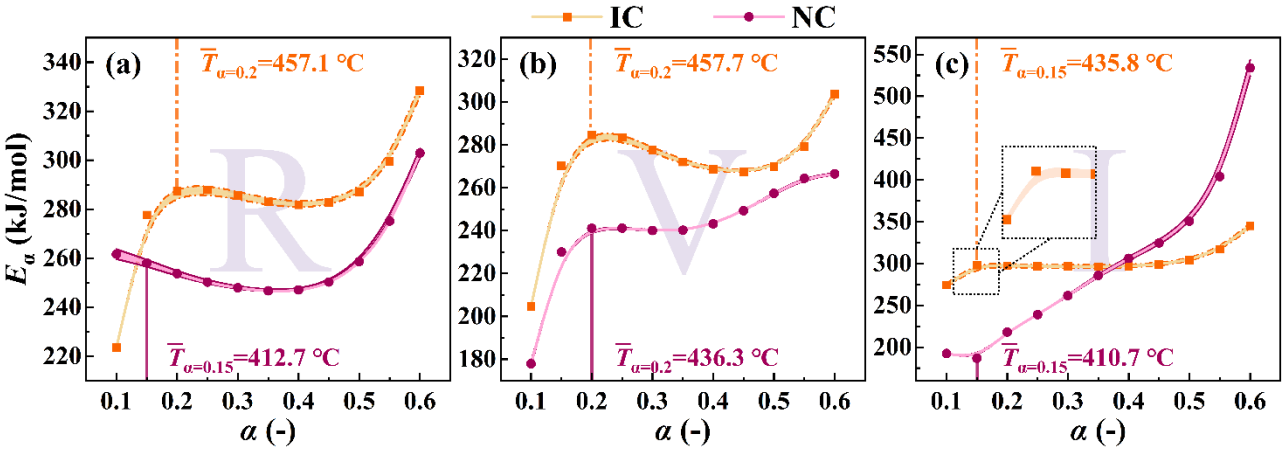

Fig. 8. The pattern of E_α with α for two coals and their macerals, the shaded area enclosed by the curve indicates the error between FWO and KAS method: (a) raw coal; (b) vitrinite; (c) inertinite.

Considering that the temperature of IC-V at this turning point is 457.7 ℃, combined with HT-CLSM and HT-SAOS observations indicating that the expanding mobility of coal deteriorates after this temperature, it can be extrapolated that the E_α reduction interval is the decomposition and solidification stage of plastic phase. The poor yield and quality of metaplast from NC-V explain its smooth segment of E_α during pyrolysis. Paralleling the two raw coals, this great difference is also reflected in inertinite of both coals. Where IC-I has consistency with the development of E_α in IC-R and IC-V, but the inflection point is earlier and the change is weaker than IC-V. It is noteworthy that both NC-I and NC-R showed similar trends, with E_α decreasing and then increasing during the reaction. Accordingly, the thermal properties of IC-R and NC-R are mainly determined by IC-V and NC-I, respectively.

Table 5 Thermodynamic parameters based on kinetic parameters derived for all samples.

Sample	Model	Parameter	α (-)											Avg	*S*
			0.1	0.15	0.2	0.25	0.3	0.35	0.4	0.45	0.5	0.55	0.6		
IC-R	FWO	ΔH (kJ/mol)	217.7	270.5	280.1	280.5	278.3	275. 8	274.6	275.5	279.7	291.9	312.0	276.8	23.80
		ΔG (kJ/mol)	149.7	158.2	163.2	166.7	169.5	172.0	174.3	176.6	178.9	181.6	184.7	170.5	10.50
		ΔS (kJ/mol)	0.1032	0.1606	0.1623	0.1551	0.1460	0.1376	0.1315	0.1281	0.1289	0.1390	0.1673	0.1418	0.01895
	KAS	ΔH (kJ/mol)	218.2	273.1	282.9	283.1	280.5	277.7	276.3	277.1	281.4	294.0	323.3	278.9	24.44
		ΔG (kJ/mol)	149.8	158.6	163.7	167.1	169.9	172.3	174.6	176.9	179.2	181.9	185.2	170.8	10.53
		ΔS (kJ/mol)	0.1037	0.1637	0.1655	0.1580	0.1486	0.1398	0.1334	0.1299	0.1307	0.1413	0.1708	0.1441	0.01981
IC-V	FWO	ΔH (kJ/mol)	199.4	263.3	277.3	276.2	270.5	265.1	261.7	260.7	262.9	272.1	295.9	264.1	23.76
		ΔG (kJ/mol)	150.2	158.5	163.4	166.9	169.8	172.3	174.5	176.8	179.1	181.7	184.7	170.7	10.38
		ΔS (kJ/mol)	0.07440	0.1497	0.1581	0.1488	0.1352	0.1231	0.1144	0.1089	0.1074	0.1142	0.1379	0.1247	0.02431
	KAS	ΔH (kJ/mol)	198.8	265.5	280.0	278.5	272.3	266.5	262.8	261.6	263.7	273.2	298.0	265.5	24.52
		ΔG (kJ/mol)	150.4	158.9	163.8	167.3	170.1	172.5	174.8	177.0	179.3	181.9	185.1	171.0	10.37
		ΔS (kJ/mol)	0.07329	0.1523	0.1611	0.1515	0.1372	0.1246	0.1154	0.1097	0.1082	0.1153	0.1401	0.1263	0.02547
IC-I	FWO	ΔH (kJ/mol)	267.3	290.6	289.6	289.3	289.0	288.8	289.3	291.4	296.4	309.0	336.4	294.3	16.95
		ΔG (kJ/mol)	148.83	157.66	162.8	166.3	169.1	171.5	173.8	176.0	178.4	181.0	184.2	170.0	10.55
		ΔS (kJ/mol)	0.1787	0.1899	0.1761	0.1675	0.1611	0.1556	0.1515	0.1495	0.1510	0.1614	0.1883	0.1664	0.01482
	KAS	ΔH (kJ/mol)	270.3	294.2	292.9	292.2	291.8	291.4	291.9	293.9	298.9	312.0	340.6	297.3	17.28
		ΔG (kJ/mol)	149.3	158.2	163.4	166.8	169.6	171.9	174.2	176.4	178.8	181.5	184.9	170.5	10.55
		ΔS (kJ/mol)	0.1825	0.1942	0.1799	0.1710	0.1643	0.1585	0.1543	0.1522	0.1537	0.1646	0.1926	0.1698	0.01541
NC-R	FWO	ΔH (kJ/mol)	255.0	251.4	247.2	243.8	241.6	240.4	240.7	243.9	252.0	268.1	295.1	252.6	16.29
		ΔG (kJ/mol)	142.1	152.9	157.7	160.8	163.2	165.3	167.3	169.3	171.4	173.9	176.9	163.7	10.08
		ΔS (kJ/mol)	0.1783	0.1459	0.1289	0.1175	0.1095	0.1037	0.1004	0.1008	0.1076	0.1239	0.1525	0.1245	0.02506
	KAS	ΔH (kJ/mol)	257.8	253.4	248.6	244.9	242.3	240.9	241.2	244.4	252.7	269.5	297.8	254.0	16.87
		ΔG (kJ/mol)	142.5	153.2	158.0	161.0	163.4	165.5	167.5	169.5	171.6	174.2	177.4	164.0	10.04
		ΔS (kJ/mol)	0.1820	0.1483	0.1306	0.1187	0.1103	0.1043	0.1008	0.1012	0.1083	0.1254	0.1553	0.1259	0.02617
NC-V	FWO	ΔH (kJ/mol)	173.4	224.1	234.9	235.0	233.9	234.0	236.9	242.9	250.8	257.6	259.6	234.8	23.14
		ΔG (kJ/mol)	142.4	154.0	159.0	162.2	164.8	167.2	169.5	171.9	174.6	177.8	181.6	165.9	11.28
		ΔS (kJ/mol)	0.04911	0.1035	0.1088	0.1024	0.09587	0.09160	0.09123	0.09470	0.1001	0.1033	0.09896	0.09445	0.01599
	KAS	ΔH (kJ/mol)	172.0	224.6	235.6	235.5	234.2	234.2	237.1	243.2	251.3	258.3	260.2	235.1	23.66
		ΔG (kJ/mol)	142.7	154.1	159.2	162.4	165.0	167.4	169.7	172.1	174.8	178.0	181.8	166.1	11.27
		ΔS (kJ/mol)	0.04646	0.1039	0.1095	0.1029	0.09601	0.09153	0.09115	0.09482	0.1005	0.1039	0.09937	0.09455	0.01692
NC-I	FWO	ΔH (kJ/mol)	187.5	181.8	212.5	232.8	255.0	278.5	298.3	316.3	341.6	393.6	520.1	292.6	99.95
		ΔG (kJ/mol)	134.0	153.2	160.6	164.7	167.8	170.6	173.3	176.0	178.7	181.1	181.5	167.4	14.15
		ΔS (kJ/mol)	0.08927	0.04260	0.07381	0.09434	0.1184	0.1439	0.1638	0.1806	0.2057	0.2622	0.4050	0.1618	0.1027
	KAS	ΔH (kJ/mol)	187.4	180.2	211.9	233.0	256.1	280.7	301.3	320.0	346.4	400.9	533.6	295.6	104.24
		ΔG (kJ/mol)	134.2	153.5	160.9	164.9	168.1	170.9	173.8	176.6	179.6	182.7	185.6	168.3	14.79
		ΔS (kJ/mol)	0.08886	0.03972	0.07260	0.09442	0.1196	0.1463	0.1671	0.1846	0.2107	0.2692	0.4162	0.1645	0.1067

Avg: average; R^2: goodness of fit; *S*: standard deviation.

We have counted the thermodynamic parameters at 5 °C/min as listed in **Table 5** and obtained positive values of ΔH, ΔG, and ΔS, which are consistent with the non-spontaneous reaction behavior of this pyrolysis process. Focusing on ΔH, ΔG, and ΔS versus conversion rate as shown in **Fig. 9**, where ΔH and ΔS of different samples exhibit regularities corresponding to E_α. The pyrolysis of the two coals and their macerals is an endothermic and chaotic process, and the specific change behavior can be explained by the differential reactions of the metaplast in the thermal active stage analyzed above. All samples demonstrate a continuous increase in ΔG, implying a high product conversion capacity of coal-based materials during the non-spontaneous reaction [52]. The samples with the largest ΔG are IC-V in the IC group and NC-I in the NC, which reaffirms their decisive influence on the chemical properties of the respective raw coals. In summary, the dissimilarity in raw coal properties is mainly controlled by the genetic regulation of maceral thermal properties.

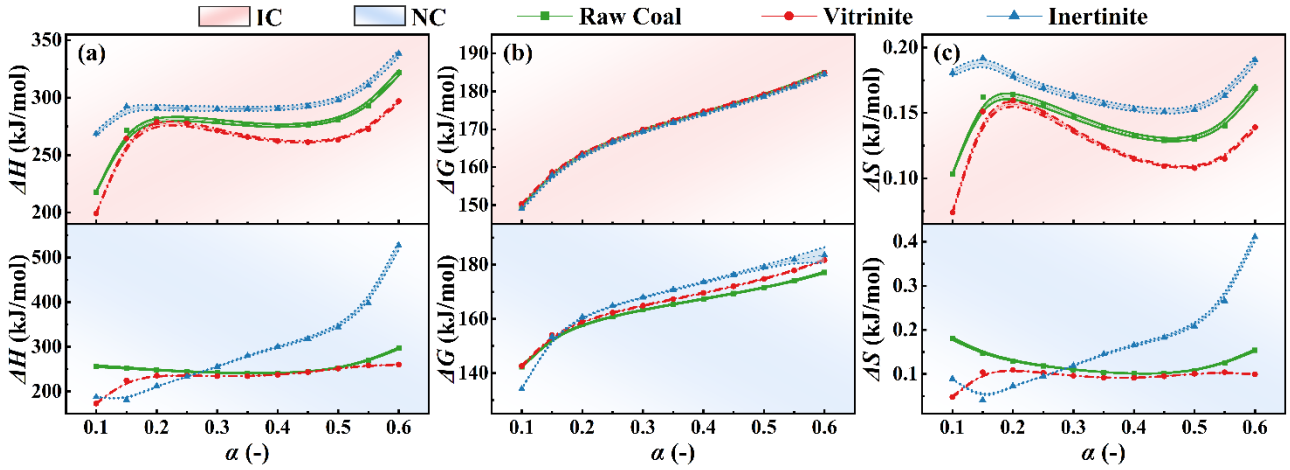

Fig. 9. The pattern of thermodynamic parameters with α for two coals and their macerals: (a) ΔH; (b) ΔG; (c) ΔS.

4. Conclusion

Based on the microscopic composition perspective of coal, this study successfully accesses the thermal expansion behavior of different coal types in the coking process and the source of their activity differences through experimental, characterization, and calculation, which has theoretical implications for the development of coal chemical production toward refinement and energy

conservation as well as to further improve the efficiency of coal classification and utilization. The specific conclusions obtained are as follows:

(1) The coking ability of raw coal depends on the quality of vitrinite and its thermal softening metaplast. Compared with the vitrinite of gas coal, the vitrinite of coking coal has superior metaplast formation, thermal decomposition resistance, and solidification ability.

(2) The thermal activity of vitrinite can be manifested in multiple ways, including thermal weightlessness, mineral catalytic potential, and product behavior compared to inertinite. The chemical structure distinctions of coal macerals are the main reason for the variations in thermal stability.

(3) Although the pyrolytic properties of raw coal and its macerals are limited by coal rank, some macerals in coal with similar kinetic and thermodynamic behavior to raw coal will genetically regulate the characteristics of coal. The properties of coking coal and gas coal are determined by vitrinite and inertinite, respectively.

Still, there are some limitations of this work that need to be addressed as follows:

(1) This work only discusses two different coal types with representative coal rank in a plant, while a mixture of multiple coals is often used in actual production. Therefore, the relevant properties of other coal ranks with different types of feedstocks are still without extensive research.

(2) Despite the revelation of the genetic relationship between the pyrolytic properties of raw coal and macerals, the quantitative relationship in the quality of coke obtained from them was not explored, and the property link between coal-based raw materials and coke was not constructed.

5. Challenges and future directions

To evaluate more precisely the quantitative relationship between the properties of raw coal and its macerals, the interaction between different components and minerals will need to be considered, which poses further challenges to the high-purity purification process of each maceral. Meantime, some unconventional but more intuitive *in-situ* methods used in this work are only applied to

459 characterize the thermal behavior of loose coal grains, and how to extend their application in coking
460 experiments with a certain bulk density will also become a direction for our future optimization
461 research.

462 ## Acknowledgements

463 The work is supported by the National Natural Science Foundation of China (Project No.
464 52074055 & 52104323), the Graduate Scientific Research and Innovation Foundation of Chongqing
465 (Project No. CYS22001), and the Chongqing Talent Program (Project No. cstc2021ycjh-
466 bgzxm0108). The authors also thank Mr. Weijun Bai (Beijing Precise Instrument Co., Ltd.) for his
467 guidance in coal petrographic identification and Mr. Jiaqi Zhang (Anton Paar (Shanghai) Trading
468 Co., Ltd) for his convenience in rheological testing.

469 ## Reference

470 [1] Wang J, Li X, Wang B, Xiong J, Li Y, Guo Y, *et al*. Emission characteristics of volatile organic compounds
471 during a typical top-charging coking process. Environmental Pollution 2022; 308: 119648. (DOI:
472 10.1016/j.envpol.2022.119648)
473 [2] Chen Y, Lee S, Tahmasebi A, Bai J, Mahoney M, Yu J. A review of the state-of-the-art research on carbon
474 structure evolution during the coking process: From plastic layer chemistry to 3D carbon structure
475 establishment. Fuel 2020; 271: 117657. (DOI: 10.1016/j.fuel.2020.117657)
476 [3] Zhang L, Wang G, Xue Q, Zuo H, She X, Wang J. Effect of preheating on coking coal and metallurgical coke
477 properties: A review. Fuel Processing Technology 2021; 221: 106942. (DOI:
478 10.1016/J.FUPROC.2021.106942)
479 [4] Sun J, Na H, Yan T, Qiu Z, Yuan Y, He J, *et al*. A comprehensive assessment on material, exergy and emission
480 networks for the integrated iron and steel industry. Energy 2021; 235: 121429. (DOI:
481 10.1016/J.ENERGY.2021.121429)
482 [5] Zhao M, Lv L, Wu J, Wang S, Zhang N, Bai Z, *et al*. Total factor productivity of high coal-consuming
483 industries and provincial coal consumption: Based on the dynamic spatial Durbin model. Energy 2022; 251:
484 123917. (DOI: 10.1016/J.ENERGY.2022.123917)

[6] Jonek-Kowalska I. Towards the reduction of CO_2 emissions. Paths of pro-ecological transformation of energy mixes in European countries with an above-average share of coal in energy consumption. Resources Policy 2022; 77: 102701. (DOI: 10.1016/j.resourpol.2022.102701)

[7] Hower JC, Eble CF, O'Keefe JMK. Phyteral perspectives: Every maceral tells a story. International Journal of Coal Geology 2021; 247: 103849. (DOI: 10.1016/J.COAL.2021.103849)

[8] Wang Y, Bai X, Wu L, Zhang Y, Qu S. The petrographic compositions of Chinese commercial coals: A national survey and statistical analysis. Fuel 2022; 310(Part B): 122323. (DOI: 10.1016/J.FUEL.2021.122323)

[9] Popa ME, Predeanu G. Coals of Romania: Geology, petrology and use. International Journal of Coal Geology 2018; 200: 103-122. (DOI: 10.1016/j.coal.2018.10.011)

[10] Sanders MM, Jubb AM, Hackley PC, Peters KE. Molecular mechanisms of solid bitumen and vitrinite reflectance suppression explored using hydrous pyrolysis of artificial source rock. Organic Geochemistry 2022; 165: 104371. (DOI: 10.1016/J.ORGGEOCHEM.2022.104371)

[11] Faiz M, Sherwood N, Wilkins RWT. Elemental composition of dispersed vitrinite in marine Jurassic source rocks of the Vulcan Sub-basin, Australia: Implications for vitrinite reflectance suppression. Marine and Petroleum Geology 2021; 133: 105278. (DOI: 10.1016/J.MARPETGEO.2021.105278)

[12] Róg L. Vitrinite reflectance as a measure of the range of influence of the temperature of a georeactor on rock mass during underground coal gasification. Fuel 2018; 224: 94-100. (DOI: 10.1016/j.fuel.2018.02.165)

[13] Wang L, Zhang H, Li Y. On the difference of characterization and supercapacitive performance of graphene nanosheets from precursors of inertinite- and vitrinite-rich coal. Journal of Alloys and Compounds 2020; 815: 152502. (DOI: 10.1016/j.jallcom.2019.152502)

[14] Dong M, Feng L, Qin B. Characteristics of coal gasification with CO_2 after microwave irradiation based on TGA, FTIR and DFT theory. Energy 2023; 267: 126619. (DOI: 10.1016/J.ENERGY.2023.126619)

[15] Lei Z, Liang Q, Ling Q, Cui P, Zhao Z. Investigating the reaction mechanism of light tar for Shenfu bituminous coal pyrolysis. Energy 2023; 263(Part B): 125731. (DOI: 10.1016/J.ENERGY.2022.125731)

[16] Zhao J, Mangi HN, Zhang Z, Chi R, Zhang H, Xian M, *et al*. The structural characteristics and gasification performance of cokes of modified coal extracted from the mixture of low-rank coal and biomass. Energy 2022; 258: 124864. (DOI: 10.1016/J.ENERGY.2022.124864)

[17] Zhang L, Hower JC, Liu W. Non-isothermal TG-DSC study on prediction of caking properties of vitrinite-

514 rich concentrates of bituminous coals. Fuel Processing Technology 2017; 156: 500-504. (DOI:
515 10.1016/j.fuproc.2016.10.017)
516 [18] Wu Z, Zhang J, Zhang B, Guo W, Yang G, Yang B. Synergistic effects from co-pyrolysis of lignocellulosic
517 biomass main component with low-rank coal: Online and offline analysis on products distribution and kinetic
518 characteristics. Applied Energy 2020; 276: 115461. (DOI: 10.1016/j.apenergy.2020.115461)
519 [19] Zhu W, Li X, Sun R, Yan Y, Liu J, Wang Z, *et al*. Microstructural evolution of coal to char after pyrolysis
520 using laser-induced breakdown spectroscopy and Raman spectroscopy. Energy 2023; 267: 126558. (DOI:
521 10.1016/J.ENERGY.2022.126558)
522 [20] Ge S, Yek PNY, Cheng Y, Xia C, Mahari WAW, Liew RK, et al. Progress in microwave pyrolysis conversion
523 of agricultural waste to value-added biofuels: A batch to continuous approach. Renewable and Sustainable
524 Energy Reviews 2021; 135: 110148. (DOI: 10.1016/j.rser.2020.110148)
525 [21] Aghbashlo M, Tabatabaei M, Nadian MH, Davoodnia V, Soltanian S. Prognostication of lignocellulosic
526 biomass pyrolysis behavior using ANFIS model tuned by PSO algorithm. Fuel 2019; 253: 189-198. (DOI:
527 10.1016/j.fuel.2019.04.169)
528 [22] Das B, Suresh A, Dash PS, Chandra S, Díaz MC, Stevens LA, *et al*. Understanding the unusual fluidity
529 characteristics of high ash Indian bituminous coals. Fuel Processing Technology 2018; 176: 258-266. (DOI:
530 10.1016/j.fuproc.2018.04.003)
531 [23] Jiao H, Wang M, Kong J, Guo J, Chang L. Effects of interactions among coals on the caking ability of blends
532 during carbonization. Journal of Analytical and Applied Pyrolysis 2019; 138: 154-160. (DOI:
533 10.1016/j.jaap.2018.12.019)
534 [24] Rzychoń M, Żogała A, Róg L. Experimental study and extreme gradient boosting (XGBoost) based
535 prediction of caking ability of coal blends. Journal of Analytical and Applied Pyrolysis 2021; 156: 105020.
536 (DOI: 10.1016/J.JAAP.2021.105020)
537 [25] Nomura S, Arima T. Influence of binder (coal tar and pitch) addition on coal caking property and coke
538 strength. Fuel Processing Technology 2017; 159: 369-375. (DOI: 10.1016/j.fuproc.2017.01.024)
539 [26] Hu W, Wang Q, Zhao X, Yang S, Wu H, Zhang S, *et al*. Relevance between various phenomena during coking
540 coal carbonization. Part 3: Understanding the properties of the plastic layer during coal carbonization. Fuel
541 2021; 292: 120371. (DOI: 10.1016/J.FUEL.2021.120371)
542 [27] Chen Y, Lee S, Tahmasebi A, Liu M, Zhang T, Bai J, *et al*. Mechanism of carbon structure transformation in

plastic layer and semi-coke during coking of Australian metallurgical coals. Fuel 2022; 315: 123205. (DOI: 10.1016/J.FUEL.2022.123205)

[28] Hui Y, Tian L, Lee S, Chen Y, Tahmasebi A, Mahoney M. A comprehensive study on the transformation of chemical structures in the plastic layers during coking of Australian coals. Journal of Analytical and Applied Pyrolysis 2020; 152: 104947. (DOI: 10.1016/j.jaap.2020.104947)

[29] Li J, Sun Z, Liang Y. Interaction of vitrinites in similar middle-rank coals during coking process. Fuel 2022; 316:123334. (DOI: 10.1016/J.FUEL.2022.123334)

[30] Yang H, Yang Y, Pisupati SV, Jin L, Li Y, Hu H. Modeling char surface area evolution during coal pyrolysis: Evolving characteristics with coal rank. Journal of Analytical and Applied Pyrolysis 2021; 156: 105110. (DOI: 10.1016/J.FUEL.2022.123334)

[31] Kreitzberg T, Wirch N, Bormann C, Pielsticker S, Hatzfeld O, Mayer J*, et al*. Thermally induced changes in microstructure and reactivity of biogenic and fossil fuel particles. Applied Energy 2019; 254: 113607. (DOI: 10.1016/j.apenergy.2019.113607)

[32] Khasraw D, Htet TT, Yang X, Degirmenci V, Hage H, Meijer K*, et al*. Gasification and structural behaviour of different carbon sources and resultant chars from rapid devolatilization for HIsarna alternative ironmaking process. Fuel 2022; 309: 122210. (DOI: 10.1016/J.FUEL.2021.122210)

[33] Shi J, Feng Z, Zhou D, Li X, Meng Q. Analysis of the permeability evolution law of in situ steam pyrolysis of bituminous coal combing with in situ CT technology. Energy 2023; 263(Part D): 126009. (DOI: 10.1016/J.ENERGY.2022.126009)

[34] Dwivedi KK, Shrivastav P, Karmakar MK, Pramanick AK, Chatterjee PK. A comparative study on pyrolysis characteristics of bituminous coal and low-rank coal using thermogravimetric analysis (TGA). International Journal of Coal Preparation and Utilization 2022; 42(1): 1-11. (DOI: 10.1080/19392699.2019.1566130)

[35] Song H, Liu G, Zhang J, Wu J. Pyrolysis characteristics and kinetics of low rank coals by TG-FTIR method. Fuel Processing Technology 2017; 156: 454-460. (DOI: 10.1016/j.fuproc.2016.10.008)

[36] Jiang Y, Zong P, Tian B, Xu F, Tian Y, Qiao Y, *et al*. Pyrolysis behaviors and product distribution of Shenmu coal at high heating rate: A study using TG-FTIR and Py-GC/MS. Energy Conversion and Management 2019; 179: 72-80. (DOI: 10.1016/j.enconman.2018.10.049)

[37] Bai H, Mao N, Wang R, Li Z, Zhu M, Wang Q. Kinetic characteristics and reactive behaviors of HSW vitrinite coal pyrolysis: A comprehensive analysis based on TG-MS experiments, kinetics models and ReaxFF MD

simulations. Energy Reports 2021; 7:1416-1435. (DOI: 10.1016/J.EGYR.2021.09.100)

[38] Ni Z. The caking properties of the vitrinite in coking coals and its coking behavior. Hebei United University, 2014. (https://kns.cnki.net/KCMS/detail/detail.aspx?dbname=CMFD201601&filename=1015808116.nh)

[39] Díaz MC, Duffy JJ, Snape CE, Steel KM. Use of high-temperature, high-torque rheometry to study the viscoelastic properties of coal during carbonization. Journal of Rheology 2007; 51(5): 895. (DOI: 10.1122/1.2754317)

[40] Steel KM, Dawson RE, Jenkins DR, Pearce R, Mahoney MR. Use of rheometry and micro-CT analysis to understand pore structure development in coke. Fuel Processing Technology 2017; 155:106-113. (DOI: 10.1016/j.fuproc.2016.04.027)

[41] Steel KM, Díaz MC, Patrick JW, Snape CE. Use of rheometry and ^{1}H NMR spectroscopy for understanding the mechanisms behind the generation of coking pressure. Energy & Fuels 2004; 18(5): 1250-1256. (DOI: 10.1021/ef034058l)

[42] Díaz MC, Steel KM, Drage TC, Patrick JW, Snape CE. Determination of the effect of different additives in coking blends using a combination of in situ high-temperature ^{1}H NMR and rheometry. Energy & Fuels 2005; 19(6): 2423–2431. (DOI: 10.1021/ef050126n)

[43] Díaz MC, Edecki L, Steel KM, Patrick JW, Snape CE. Determination of the effects caused by different polymers on coal fluidity during carbonization using high-temperature ^{1}H NMR and rheometry. Energy & Fuels 2008; 22(1): 471–479. (DOI: 10.1021/ef7004628)

[44] Aziz H, Rodrigues S, Esterle JS, Steel KM. Interactions between vitrinite and solid additives including inertinite during pyrolysis for coke-making considerations. Fuel Processing Technology 2020; 201:106321. (DOI: 10.1016/j.fuproc.2019.106321)

[45] Aziz H, Congo T, Steel KM. Understanding the multiple interactions of inertinite during pyrolysis/carbonisation with vitrinite: A study of two Australian coals of different rank. Fuel Processing Technology 2021; 217:106823. (DOI: 10.1016/J.FUPROC.2021.106823)

[46] Kuang Y, Zhang L, Wu L, Liu X, Wei Z, Chen J*, et al*. Insight into the separation mechanism of coal macerals by micro characterization and density functional theory calculation. Fuel 2023; 332(Part 1): 126068. (DOI: 10.1016/J.FUEL.2022.126068)

[47] Xu B, Kuang D, Liu F, Lu W, Goroncy AK, He T, *et al*. Characterization of Powder River Basin coal pyrolysis with cost-effective and environmentally-friendly composite Na-Fe catalysts in a thermogravimetric analyzer

and a fixed-bed reactor. International Journal of Hydrogen Energy 2018; 43(14): 6918-6935. (DOI: 10.1016/j.ijhydene.2018.02.102)

[48] He Y, Chang C, Li P, Han X, Li H, Fang S, *et al*. Thermal decomposition and kinetics of coal and fermented cornstalk using thermogravimetric analysis. Bioresource Technology 2018; 259: 294-303. (DOI: 10.1016/j.biortech.2018.03.043)

[49] Nisar J, Ali G, Shah A, Shah MR, Iqbal M, Ashiq MN, *et al*. Pyrolysis of Expanded Waste Polystyrene: Influence of Nickel-Doped Copper Oxide on Kinetics, Thermodynamics, and Product Distribution. Energy & Fuels 2019; 33(12): 12666-12678. (DOI: 10.1021/acs.energyfuels.9b03004)

[50] Merdun H, Laougé ZB. Kinetic and thermodynamic analyses during co-pyrolysis of greenhouse wastes and coal by TGA. Renewable Energy 2021; 163: 453-464. (DOI: 10.1016/j.renene.2020.08.120)

[51] Song Q, Zhao H, Ma Q, Yang L, Ma L, Wu Y, *et al*. Catalytic upgrading of coal volatiles with Fe_2O_3 and hematite by TG-FTIR and Py-GC/MS. Fuel 2022; 313: 122667. (DOI: 10.1016/J.FUEL.2021.122667)

[52] Gupta S, Gupta GK, Mondal MK. Thermal degradation characteristics, kinetics, thermodynamic, and reaction mechanism analysis of pistachio shell pyrolysis for its bioenergy potential. Biomass Conversion and Biorefinery 2022; 12: 4847-4861. (DOI: 10.1007/s13399-020-01104-2)

[53] Kundu N, Biswas P, Bhunia P, Ghosh R, Sarkar S. Evolution characteristics of metallurgical coals for coke making through thermogravimetric-mass spectroscopic measurements. Journal of Environmental Chemical Engineering 2021; 9(6): 106874. (DOI: 10.1016/J.JECE.2021.106874)

[54] Cheng X, Shi L, Liu Q, Liu Z. A study on vitrinite and inertinite interaction in pyrolysis of 3 coals. Journal of Analytical and Applied Pyrolysis 2021; 156: 105134. (DOI: 10.1016/J.JAAP.2021.105134)

[55] Florentino-Madiedo L, Vega MF, Díaz-Faes E, Barriocanal C. Evaluation of synergy during co-pyrolysis of torrefied sawdust, coal and paraffin. A kinetic and thermodynamic study. Fuel 2021; 292: 120305. (DOI: 10.1016/J.FUEL.2021.120305)

[56] Ling P, Xu J, Liu T, An X, Wang X, Mostafa ME, *et al*. Pyrolysis kinetics and reaction mechanisms of coal slime for cleaner energy. Journal of Analytical and Applied Pyrolysis 2022; 168: 105718. (DOI: 10.1016/J.JAAP.2022.105718)